Available online at www.sciencedirect.com
SCIENCE DIRECT®
International Journal of Heat and Mass Transfer 48 (2005) 749–764
International Journal of HEAT and MASS TRANSFER
www.elsevier.com/locate/ijhmt

Axial development of interfacial structure of vertical downward bubbly flow

Takashi Hibiki [a,b], Hiroshi Goda [b], Seungjin Kim [b], Mamoru Ishii [b,*], Jennifer Uhle [c]

[a] Research Reactor Institute, Kyoto University, Kumatori, Sennan, Osaka 590-0494, Japan
[b] School of Nuclear Engineering, Purdue University, 400 Central Drive, West Lafayette, IN 47907-2017, USA
[c] Division of System Analysis and Regulatory Effectiveness Office of Research, US Nuclear Regulatory Commission, Washington, DC 20555, USA

Received 2 February 2004
Available online 6 November 2004

Abstract

Accurate prediction of the interfacial area concentration is essential to successful development of the interfacial transfer terms in the two-fluid model. Mechanistic modeling of the interfacial area concentration entirely relies on accurate local flow measurements over extensive flow conditions and channel geometries. From this point of view, accurate measurements of flow parameters such as void fraction, interfacial area concentration, and interfacial velocity were performed by a multi-sensor probe at three axial locations as well as seven radial locations in vertical downward bubbly flows using a 25.4 mm-diameter pipe. In the experiment, the superficial liquid velocity and the void fraction ranged from −1.25 to −3.11 m/s and from 1.61% to 21.0%, respectively.

Keywords: Interfacial area transport; Two-fluid model; Downward bubbly flow; Interfacial area concentration; Resistivity multi-sensor probe; Multi-phase flow

1. Introduction

Multi-phase flow occurs in a large number of engineering systems including nuclear reactors as well as in many natural phenomena. Since the most dominant characteristic of multi-phase flow is the presence of one or several interfaces between the phases, many of two-phase systems have common topographic structure of interface. Multi-phase flow can be classified according to the geometry of the interface into different classes which are called flow regimes. The concept to two-phase flow regimes requires an introduction of a macroscopic system length scale within that the regimes are defined. For example, for slug or annular flow this length scale should be a pipe diameter. Therefore, the introduction of the flow regimes and regime dependent models lead to an analysis which can not mechanistically address the physics and transport phenomena occurring below this length scale. This leads to the necessity of phenomenological models or ad hoc models which are strongly empirical in nature and system specific. Thus, the concept of two-phase flow regimes and regime dependent models present a number of problems, ambiguity and

* Corresponding author.
E-mail addresses: hibiki@rri.kyoto-u.ac.jp (T. Hibiki), ishii@ecn.purdue.edu (M. Ishii).

0017-9310/$ - see front matter © 2004 Elsevier Ltd. All rights reserved.
doi:10.1016/j.ijheatmasstransfer.2004.07.045

Nomenclature

A	area of flow channel
a_i	interfacial area concentration
$a_{i,\mathrm{eq}}$	interfacial area concentration under conditions of no phase change and equilibrium of bubble coalescence and breakup rates
C_0	distribution parameter
D	pipe diameter
$D_{\mathrm{d,max}}$	maximum distorted bubble limit
D_{H}	hydraulic equivalent diameter of flow channel
D_{Sm}	Sauter mean diameter
g	gravitational acceleration
j	mixture volumetric flux
j_{g}	superficial gas velocity
$j_{\mathrm{g,0}}$	inlet superficial gas velocity reduced at atmospheric pressure and 20 °C
j_{f}	superficial liquid velocity
L	pipe length
Lo	Laplace length
P	pressure
R	pipe radius
Re^*	bubble Reynolds number
Re_{f}	Reynolds number
r	radial coordinate
t	time
v_i	interfacial velocity
v_{g}	average center-of-volume velocity of gas phase, or gas velocity
z	axial coordinate

Greek symbols

α	void fraction
α_2	void fraction of group-II bubble
$\Delta\rho$	density difference
ε	energy dissipation rate per unit mass
η_{ph}	void generation term due to phase change
ν_{f}	kinematic viscosity of liquid phase
ξ	interfacial area change due to bubble coalescence or breakup
ρ_{g}	gas density
ρ_{f}	liquid density
ρ_{m}	mixture density
σ	interfacial tension
ϕ_j	source and sink terms due to bubble interaction mechanisms
ϕ_{ph}	source and sink terms due to phase change

Subscripts

*	non-dimensionalized quantity
+	reference axial location

Mathematical symbols

$\langle\ \rangle$	area-averaged quantity
$\langle\langle\ \rangle\rangle$	void fraction weighted cross-sectional area-averaged quantity
$\langle\langle\ \rangle\rangle_{\mathrm{a}}$	interfacial area concentration weighted cross-sectional area-averaged quantity

difficulties, when they are applied to various actual systems.

The above discussion indicates the origin of the difficulties encountered in developing broad understanding of multi-phase flow and generalized method for analyzing such flow. The multi-phase flow physics are fundamentally multi-scale in nature. It is necessary to take into account these cascading effects of various physics at different scales in the multi-phase flow formulation and closure relations. At least four different scales can be important in multi-phase flow: These are (1) system scale, (2) macroscopic scale required for continuum assumption, (3) meso-scale related to local structures, and (4) microscopic scale related to fine structures and molecular transport. At the highest level, the scale is the system where system transients and component interactions are the primary focus. For example, nuclear reactor accidents and transient analysis requires specialized system analysis codes. At the next level, macrophysics such as the structure of interface and the transport of mass, momentum and energy are addressed. However, the multi-phase flow field equations which describe the conservation principles require additional constitutive relations for bulk transfer such as the turbulence effects for momentum and energy as well as for interfacial exchanges for mass, momentum and energy transfer. These are meso-scale physical phenomena that require concentrated research efforts. Since the interfacial transfer rates can be considered as the product of the interfacial flux and the available interfacial area, the modeling of the interfacial area concentration is essential. In two-phase flow analysis the void fraction and the interfacial area concentration represent the two fundamental first-order geometrical parameters, and therefore they are closely related to two-phase flow regimes. However, the concept of the two-phase flow regimes is difficult to quantify mathematically at the local point, because it is often defined at the scale close to the system scale. This may indicate that the modeling of the changes of the interfacial area concentration directly by a transport equation, namely interfacial area transport equation, is a better approach than the conventional method using

the flow regime transition criteria and regime dependent constitutive relations for interfacial area concentration [1,2]. This is particularly true for a three-dimensional formulation of multi-phase flow. The next lower level physics in multi-phase flow is related to the local micro-scale phenomena such as the wall nucleation or condensation.

In view of the great importance of the two-fluid model for two-phase flow analyses, considerable efforts have been devoted to develop the interfacial area transport equation [3–6], and extensive experimental works for vertical cocurrent upward flows have been performed [7–11]. In addition to the study of upward two-phase flow, study of downward two-phase flow is also important in view of nuclear reactor safety analysis and chemical and petroleum plant design. In particular, downward two-phase flow is observed in light water reactor accident scenarios, such as loss of heat sink by feed water loss or secondary pipe break. In such scenario, cocurrent downward two-phase flow may occur in steam generator. It is also possible that the two-phase flow may go through the steam generator in cases of small break loss of coolant accident or relief valve open, and thus creating both cocurrent upward and downward flows. From this point of view, the experimental work has been initiated to measure the axial interfacial area transport in vertical cocurrent downward flows using a 50.8-mm diameter pipe [12]. To complete the basic database of cocurrent downward flow, this study is also aiming at the measurement of the axial development of local flow parameters for cocurrent downward bubbly flows in a 25.4-mm diameter pipe by means of a conductivity multi-sensor probe. The parameters obtained in this study include void fraction, interfacial area concentration, bubble Sauter mean diameter and interfacial velocity. The data from the multi-sensor probe give sufficient information to evaluate the interfacial area transport equation.

2. Interfacial area transport equation

The foundations of the interfacial area transport equation were first established by Kocamustafaogullari and Ishii [2]. The general form of the three-dimensional interfacial area transport equation is given by

$$\frac{\partial a_i}{\partial t}+\nabla\cdot(a_i\vec{v}_i)=\frac{2}{3}\left(\frac{a_i}{\alpha}\right)\left\{\frac{\partial\alpha}{\partial t}+\nabla\cdot\left(\alpha\vec{v}_g\right)-\eta_{ph}\right\}+\sum_j\phi_j+\phi_{ph},\quad(1)$$

where a_i, t, $\vec{v}_i$, α, and $\vec{v}_g$ are the interfacial area concentration, the time, the interfacial velocity, the void fraction, and the average center-of-volume velocity of the gas phase, respectively. The first term on the right hand side of Eq. (1) represents the source term in the interfacial area concentration due to change in the void fraction. This term includes the void generation due to phase change, η_{ph} The terms ϕ_j and ϕ_{ph} represent the source and sink terms due to the bubble interaction mechanisms and phase change, respectively. In order to complete the interfacial area transport model, constitutive relations for the source and sink terms appearing in the interfacial area transport equation have to be developed. This is achieved by mechanistically modeling the bubble interaction mechanisms in a two-phase flow. Some attempts have been made to model the source and sink terms in the interfacial area transport equation of vertical upward bubbly flows in pipes [3–6]. Under an adiabatic flow condition, the interfacial area transport equation can be simplified to

$$\frac{\partial a_i}{\partial t}+\nabla\cdot(a_i\vec{v}_i)=\frac{2}{3}\left(\frac{a_i}{\alpha}\right)\left\{\frac{\partial\alpha}{\partial t}+\nabla\cdot\left(\alpha\vec{v}_g\right)\right\}+\sum_j\phi_j.\quad(2)$$

Under a steady adiabatic flow condition, the interfacial area transport equation can be further simplified to

$$\nabla\cdot(a_i\vec{v}_i)=\frac{2}{3}\left(\frac{a_i}{\alpha}\right)\nabla\cdot\left(\alpha\vec{v}_g\right)+\sum_j\phi_j.\quad(3)$$

For a steady adiabatic one-dimensional flow at the equilibrium state of bubble interaction ($\sum_j\phi_j=0$), the interfacial area transport equation is reduced to the most simplified form as

$$\frac{\partial}{\partial z}(a_iv_i)=\frac{2}{3}\left(\frac{a_i}{\alpha}\right)\frac{\partial}{\partial z}\left(\alpha v_g\right).\quad(4)$$

This most simplified interfacial area transport equation clearly indicates that the interfacial area concentration varies along the flow direction due to the bubble volume change by the pressure change even in a steady adiabatic one-dimensional flow at the equilibrium state of bubble interaction.

3. Experimental

Fig. 1 shows the schematic diagram of the two-phase flow loop. The test loop consisted of two test sections, which were acrylic pipes with inner diameters of 25.4 and 50.8 mm, whose total lengths, L, non-dimensionalized by the pipe diameter, D, were $L/D=150$ and 75, respectively. In the present experiment, the flow channel with an inner diameter of 25.4 mm was utilized.

Air was supplied by a compressor, and was introduced into a mixing chamber through a porous media with the pore size of 10 μm. The air and purified water were mixed in the mixing chamber, and the mixture flowed downward through the test section. The flow rates of the air and water were measured with a rotameter and a magnetic flow meter, respectively. The accuracies

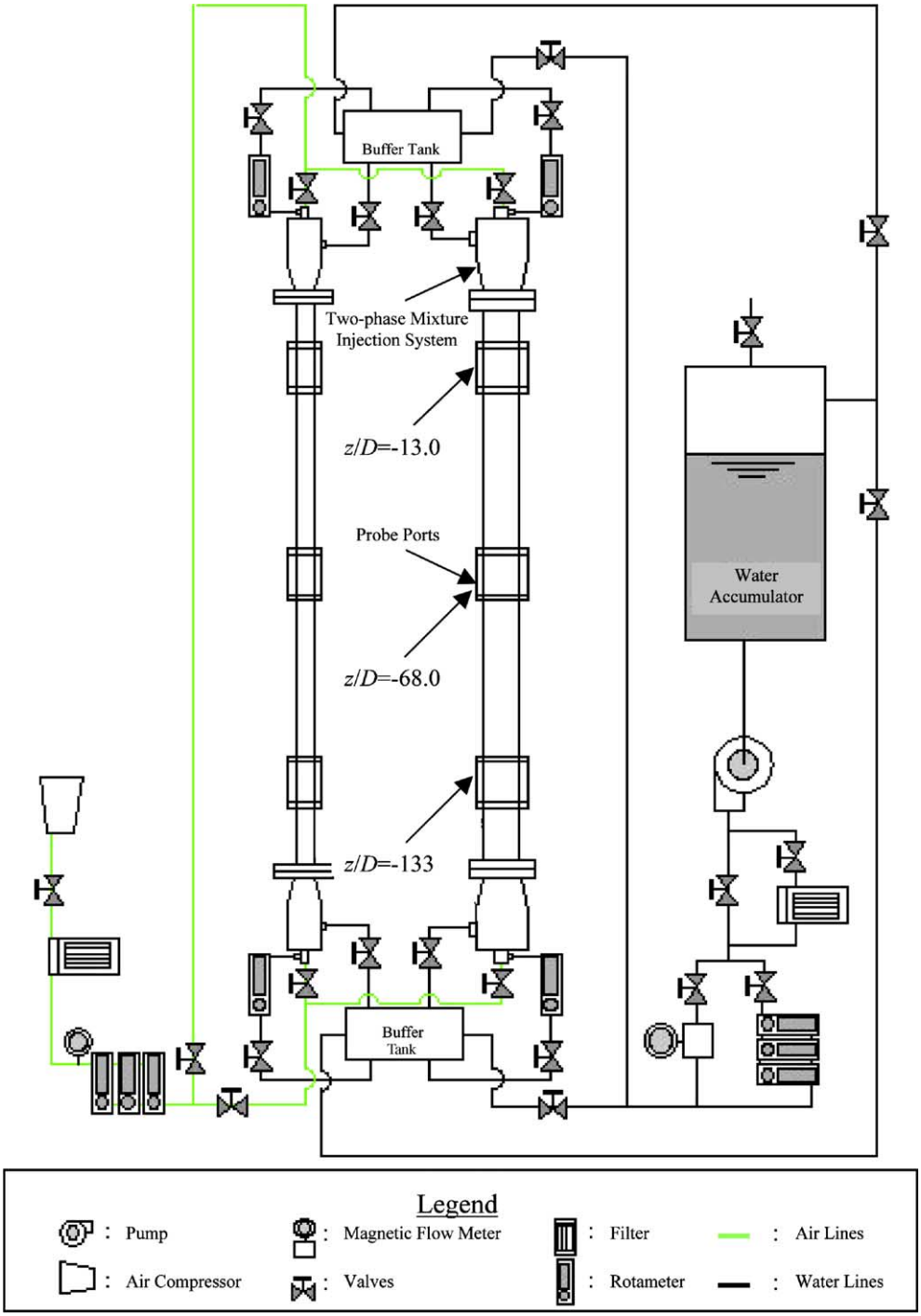

Fig. 1. Schematic diagram of experimental loop.

of the gas rotameter and the magnetic flow meter are within ±4% and ±1% of full scale, respectively. The pressure and differential pressure measurements were also conducted by a pressure gauge at the test section inlet and a differential pressure transducer at three probe ports, respectively. The accuracies of the pressure gauge and the pressure transducer are within ±3% of span and within ±1% of full scale, respectively. The local flow

Table 1
Flow conditions in this experiment

Symbols	●	▲	■
Lines	—	---	···
$\langle j_f \rangle$ [m/s]	$\langle j_{g,0} \rangle$ [m/s]	$\langle j_{g,0} \rangle$ [m/s]	$\langle j_{g,0} \rangle$ [m/s]
−1.25 ($\langle \alpha \rangle_{z/D=-13.0}$ [%])	−0.0177(1.61)[a]	−0.0993 (7.59)[a]	−0.289[b] (21.0)[a]
−2.12 ($\langle \alpha \rangle_{z/D=-13.0}$ [%])	−0.102 (4.70)[a]	−0.381[b] (17.2)[a]	N/A
−3.11 ($\langle \alpha \rangle_{z/D=-13.0}$ [%])	−0.106 (2.80)[a]	−0.487[b] (12.7)[a]	N/A

N/A = Not available.
[a] Values in parentheses mean the void fractions in % measured at $z/D = -13.0$.
[b] Group-II bubbles were observed in these flow conditions.

parameters such as void fraction, interfacial area concentration, and interfacial velocity were measured by using a multi-sensor conductivity probe at three axial locations of $z/D = -13.0$, -68.0, and -133 and seven radial locations from $r/R = 0$ to 0.9. Here, negative z/D means vertically downward location measured from the test section inlet ($z/D = 0$), and the radial locations of the pipe center and wall are represented by $r/R = 0$ and $r/R = 1$, respectively. The flow conditions in this experiment are tabulated in Table 1. It should be noted here that a negative sign for superficial gas velocity, $\langle j_{g,0} \rangle$, and superficial liquid velocity, $\langle j_f \rangle$, means downward flow. The experiments were performed at 7 flow conditions and a total of 147 (= 7 flow conditions × 7 radial locations × 3 axial locations) local data were acquired.

The multi-sensor conductivity probe methodology is detailed in our previous paper [13]. The void fraction, interfacial area concentration and gas velocity obtained by area-averaging local flow parameters measured by the sensor method agreed with those measured by other calibrators such as a gamma densitometer, a photograph, and a rotameter within ±5.74% [8,9], ±6.95% [8,9], and ±7.51%, respectively. Local profiles of void fraction and interfacial area concentration measured by the sensor method also agreed with those measured by the stereo-imaging method very well [14]. Thus, it can be considered that the measurement accuracy of flow parameters would be within ±15% as a conservative estimate [12]. Error bars in figures to be shown later indicate the error band within ±15%.

In the characteristic transport phenomenon in bubbly flow including bubbly-to-slug transition flow, the characteristic drag of spherical and distorted bubbles is significantly different from that of cap and slug bubbles. Hereafter, the former and latter bubble groups refer to group-I and group-II bubbles, respectively. Such bubble categorization is important because multiple transport equations such as two-group interfacial area transport equations [5,6] should be employed to describe the fluid particle transport at the flow condition where the group-II bubbles are formed. The bubble groups can be categorized based on the maximum distorted bubble limit, $D_{d,max}$ given by [15]

$$D_{d,max} = 4\sqrt{\frac{\sigma}{g\Delta\rho}}, \tag{5}$$

where σ, g, and $\Delta\rho$ are the surface tension, the gravitational acceleration, and the density difference, respectively. For an air-water flow at atmospheric pressure (0.101 MPa) and room temperature (20.0 °C), the maximum distorted bubble size was estimated to be 10.9 mm. This categorization was approximately made by measured bubble chord length. The methodology is detailed in our previous paper [16]. It should be noted here that Eq. (5) is not applicable to a flow in a channel with a diameter smaller than $D_{d,max}$.

4. Results and discussion

4.1. Initial bubble size

Axial developments of local profiles of flow parameters in bubbly flows significantly depend on an initial condition such as initial bubble size. Since the bubble size controlling function was not implemented in the current bubble distributor, the initial bubble size was not kept constant in this experiment, resulting in the dependence of the initial bubble size on the flow condition. The upper and lower figures in Fig. 2 show the dependences of the bubble size measured near the inlet, $z/D = -13.0$ on the void fraction and the superficial liquid velocity, respectively. Open symbols in the upper figure indicate the measured bubble size. Lines in lower figure indicate the bubble size reproduced by the interpolation of the data shown in upper figure. Both gas and liquid flow rates increase the bubble size near the inlet, which means that they mainly enhance the bubble coalescence due to the bubble collision near the inlet.

4.2. Void fraction

Local void fraction, α, profiles measured at $z/D = -13.0$, -68.0 and -133 are, respectively, depicted in the upper, middle and lower figures in Fig. 3. Axial developments of one-dimensional total void fractions, $\langle \alpha \rangle$, and group-II void fractions, $\langle \alpha_2 \rangle$, are also shown

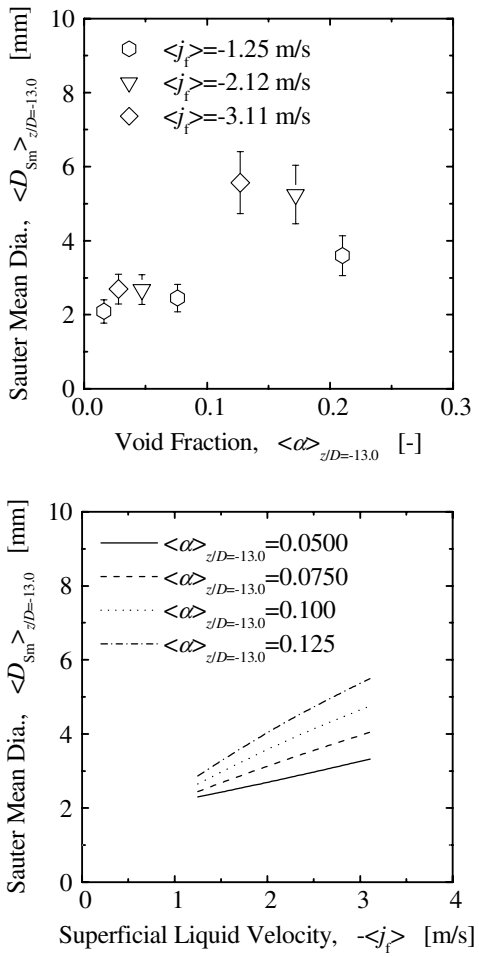

Fig. 2. Dependence of initial bubble size on void fraction and superficial liquid velocity.

in the upper and lower figures in Fig. 4. The meanings of the symbols are tabulated in Table 1. The lines in Fig. 4 indicate the values calculated by the following drift-flux model [17].

$$\left\langle\left\langle v_g^*\right\rangle\right\rangle = C_0\langle j^*\rangle + 1, \quad \text{where}$$
$$\left\langle\left\langle v_g^*\right\rangle\right\rangle = \langle\langle v_g\rangle\rangle/V_{gj} \text{ and } \langle j^*\rangle = \langle j\rangle/V_{gj}. \tag{6}$$

Here, $\langle\langle\ \rangle\rangle$ means the void-fraction weighted cross-sectional area-averaged quantity. The distribution parameter, C_0 and the drift velocity, V_{gj} are given by

$$C_0 = (-0.0214\langle j^*\rangle + 0.772) + (0.0214\langle j^*\rangle + 0.228)\sqrt{\frac{\rho_g}{\rho_f}} \quad \text{for } -20 \leqslant \langle j^*\rangle \leqslant 0,$$
$$C_0 = \left(0.2e^{0.00848(\langle j^*\rangle+20)} + 1.0\right) - 0.2e^{0.00848(\langle j^*\rangle+20)}\sqrt{\frac{\rho_g}{\rho_f}} \quad \text{for } \langle j^*\rangle < -20, \tag{7}$$

$$V_{gj} = \sqrt{2}\left(\frac{g\sigma\Delta\rho}{\rho_f^2}\right)^{1/4}, \tag{8}$$

where ρ_g, ρ_f and j are the gas density, the liquid density, and the mixture volumetric flux, respectively.

The void fraction profiles observed in the present experiments using a 25.4-mm diameter pipe are quite similar to those in a 50.8-mm diameter pipe [12]. The void fraction profiles may be characterized as follows.

(1) Unlike upward flows, no significant wall peaking phenomenon is observed in downward flows.
(2) A bubble-free region near the channel wall is observed in downward flows.
(3) No significant axial change is observed in the void fraction profile at the flow conditions where no group-II bubble is formed.
(4) As the flow develops, the bubbles localized around the channel center tend to be redistributed over the flow channel at the flow conditions where group-II bubbles are formed ($\langle j_{g,0}\rangle = -0.289$ m/s and $\langle j_f\rangle = -1.25$ m/s, $\langle j_{g,0}\rangle = -0.381$ m/s and $\langle j_f\rangle = -2.12$ m/s, $\langle j_{g,0}\rangle = -0.487$ m/s and $\langle j_f\rangle = -3.11$ m/s).

The observations (1) and (2) may be approximately explained by forces acting on bubbles. Typical non-drag forces modeled are lift force [18,19], wall repulsion force [20], and turbulent dispersion force [21]. The lift force is in proportional to the gradient of the relative velocity between phases, and thus, tends to move bubbles towards channel wall and center directions in upward and downward flows, respectively. The wall repulsion force acts on a bubble near a wall, and prevents the bubbles from touching the wall. Thus, the wall repulsion force always tends to move bubbles towards channel center direction. The turbulent dispersion force is driven by the void fraction gradient, and tends to uniformize the void fraction distribution. Thus, the force balance among these three forces causes no significant wall peaking in the void fraction profile and a bubble-free region near the channel wall. The bubble-free region near the channel wall was also observed by Kashinski and Randin [22].

The observations (3) and (4) may be approximately explained by bubble interaction processes. If the initial bubble size is too small or too large in comparison with the equilibrium size, the bubbles eventually tend to reach the equilibrium state in size though the bubble interactions such as coalescence and breakup. However, for relatively low void fraction and liquid velocity where no group-II bubble is formed, the driving force for the bubble interaction may not be strong enough to attain the equilibrium state in bubble size within the limited test section length. This leads to no significant axial change in the void fraction profile. For the flow conditions where group-II bubbles are formed at the inlet, the

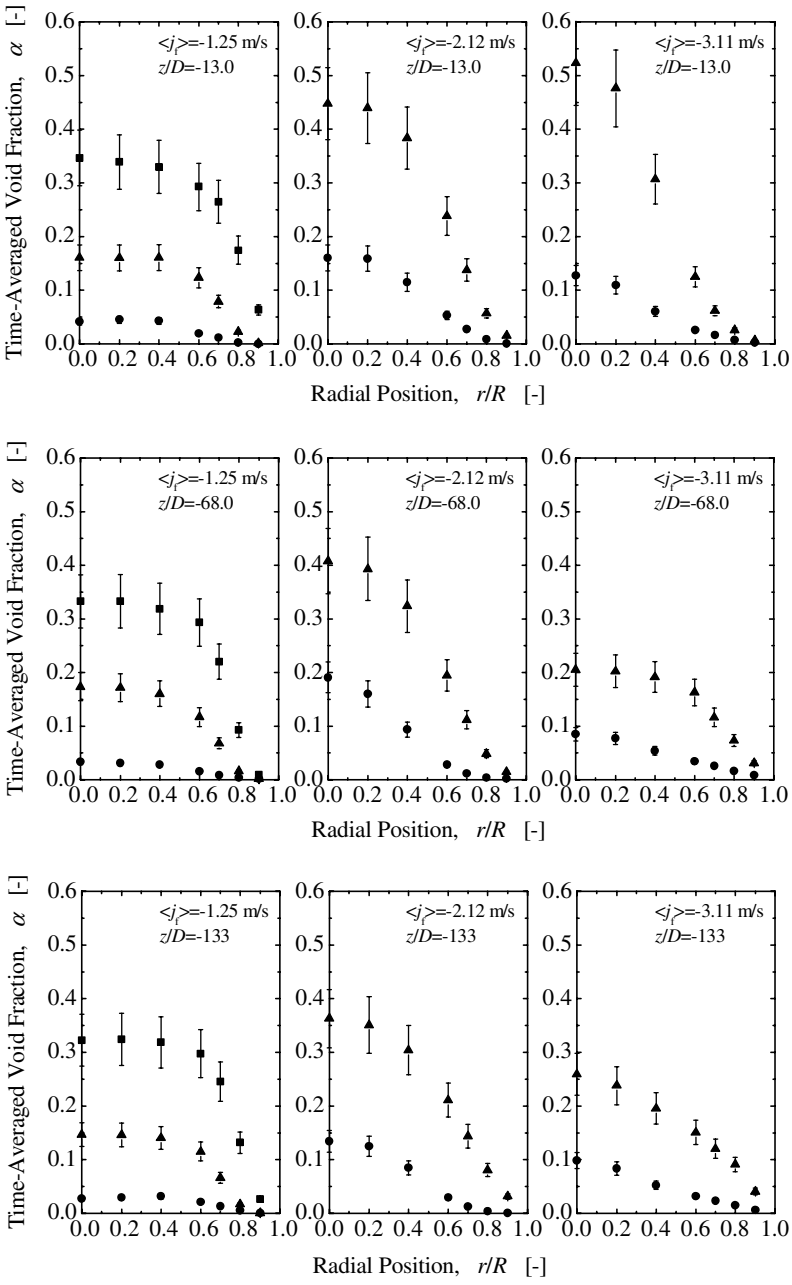

Fig. 3. Local void fraction profiles at $z/D = -13.0$, -68.0 and -133.

mechanism of axial change in the flow structure may be classified into two typical patterns in terms of the liquid turbulence. If the liquid turbulence is not high enough to disintegrate the formed cap bubbles near the inlet, it may mainly enhance the bubble fluctuation resulting in enhanced bubble coalescence. Then, the cap bubble size increases along the flow direction, and growing cap bubbles uniformize the void profile around the channel center due to their relatively flat shape resulting in the reduction of the void fraction around the channel center. If the liquid turbulence is high enough, it may disintegrate the formed cap bubbles near the inlet. Then, the disintegrated cap bubbles may more or less redistributed around the flow channel resulting in the uniformization of the void profile and the reduction of the void fraction around the channel center. This speculation agrees with the data tendency shown in Fig. 3 and the lower figure of Fig. 4.

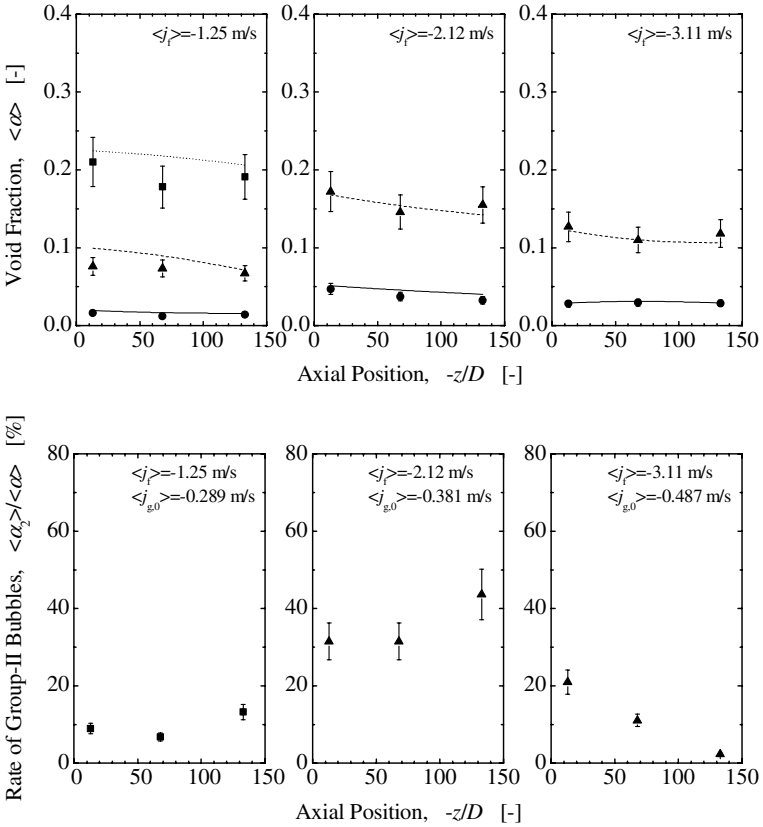

Fig. 4. Axial development of one-dimensional void fraction and rate of group-II void fraction.

As shown in the upper figure of Fig. 4, the one-dimensional total void fraction decreases along the flow direction mainly due to the pressure increase. The drift-flux model [17] developed based on fully-developed flow data also reproduce the axial developments of the void fraction very well. The averaged prediction accuracy is estimated to be within ±9.66%. This indicates the drift-flux model given by Eqs. (6)–(8) can be applicable even to developing flows.

4.3. Interfacial area concentration

Local interfacial area concentration, a_i profiles measured at $z/D = -13.0$, -68.0 and -133 are, respectively, depicted in the upper, middle and lower figures in Fig. 5. Axial developments of one-dimensional total interfacial area concentrations, $\langle a_i \rangle$, are also shown in Fig. 6. The meanings of the symbols are tabulated in Table 1. The lines in Fig. 6 indicate the values calculated by the following interfacial area correlation developed based on data taken in various forced-convective upward bubbly flows and bubble columns [23].

$$a_i^* = 3.02 Lo^{*0.335} \alpha Re^{*0.239} \text{ or}$$
$$D_{Sm}^* = 1.99 Lo^{*-0.335} Re^{*-0.239}, \tag{9}$$

where the non-dimensional interfacial area concentration, a_i^* Laplace length scale, Lo, non-dimensional Laplace length scale, Lo^* and Reynolds number, Re^* are defined as follows:

$$a_i^* \equiv a_i Lo, \quad Lo \equiv \sqrt{\frac{\sigma}{g\Delta\rho}}, \quad Lo^* \equiv \frac{Lo}{D_H},$$
$$Re^* \equiv \frac{(\varepsilon^{1/3} Lo^{1/3}) Lo}{\nu_f}. \tag{10}$$

Here, D_H and ν_f are the hydraulic equivalent diameter and the kinematic viscosity of the liquid phase, respectively. The energy dissipation rate per unit mass, ε, may be approximately determined by [23]

$$\varepsilon = g \mid \langle j_g \rangle \mid \exp(-0.0005839 Re_f) + \frac{\mid \langle j \rangle \mid}{\rho_m} \left(-\frac{dP}{dz} \right)_F \times \{1 - \exp(-0.0005839 \mathrm{Re}_f)\}, \tag{11}$$

where ρ_m, Re_f and $(-dP/dz)_F$ are, respectively, the mixture density, the liquid Reynolds number defined by $\langle j_f \rangle D_H/\nu_f$, and the pressure loss per unit length due to friction. It should be noted here that Eq. (9) is not applicable to the flow conditions where group-II bubbles are formed.

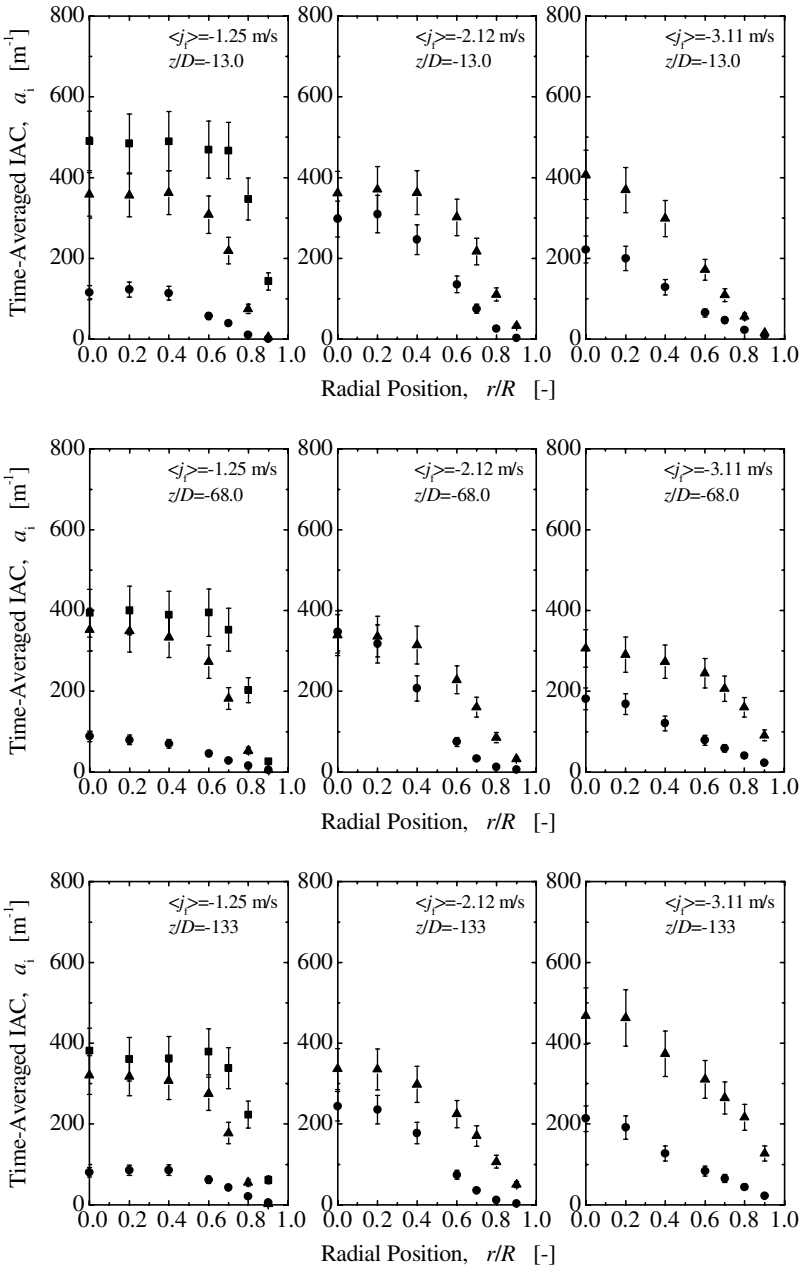

Fig. 5. Local interfacial area concentration profiles at $z/D = -13.0$, -68.0 and -133.

The interfacial area concentration profiles observed in the present experiments using a 25.4-mm diameter pipe are quite similar to those in a 50.8-mm diameter pipe [12]. The interfacial area concentration profiles may be characterized as follows:

(1) Unlike upward flows, no significant wall peaking phenomenon is observed in downward flows.
(2) The interfacial area concentration profiles are similar to the void fraction profiles at the flow conditions where no group-II bubble is formed.
(3) No significant axial change is observed in the interfacial area concentration profile at the flow conditions where no group-II bubble is formed.
(4) Axial changes are observed in the interfacial area concentration profile at the flow conditions where

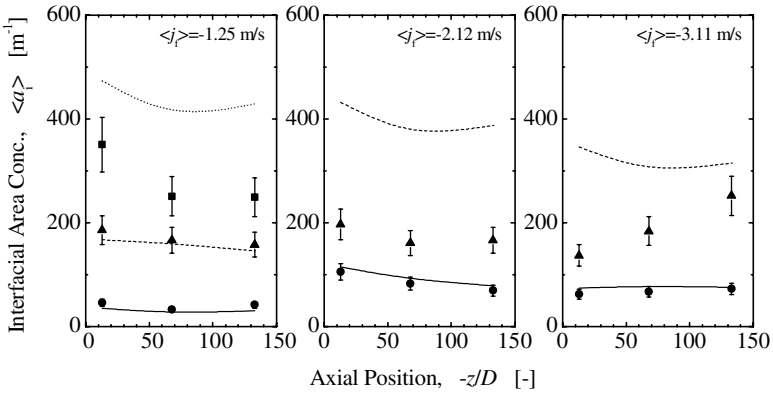

Fig. 6. Axial development of one-dimensional interfacial area concentration.

group-II bubbles are formed ($\langle j_{g,0}\rangle = -0.289$ m/s and $\langle j_f\rangle = -1.25$ m/s, $\langle j_{g,0}\rangle = -0.381$ m/s and $\langle j_f\rangle = -2.12$ m/s, $\langle j_{g,0}\rangle = -0.487$ m/s and $\langle j_f\rangle = -3.11$ m/s).

The observations (1) and (2) may be approximately explained by the geometrical relationship between void fraction and interfacial area concentration. The interfacial area concentration is basically proportional to the void fraction and inversely proportional to the bubble Sauter mean diameter. As explained later, the bubble Sauter mean diameters are almost uniform along the channel radius at the flow conditions. Thus, the interfacial area concentration profiles show the same behavior as their respective void fraction profiles.

As already explained in Section 4.2, the observations (3) and (4) may be approximately explained by bubble interaction processes. This speculation agrees with the data tendency shown in Figs. 5 and 6.

As shown in Fig. 6, the one-dimensional interfacial area concentration decreases along the flow direction mainly due to the pressure increase and the cap bubble formation in the tested flow conditions except for $\langle j_{g,0}\rangle = -0.487$ m/s and $\langle j_f\rangle = -3.11$ m/s. For $\langle j_{g,0}\rangle = -0.487$ m/s and $\langle j_f\rangle = -3.11$ m/s, the disintegration of cap bubbles due to strong liquid turbulence increases the interfacial area concentration along the flow direction. The applicability of the interfacial area correlation given by Eq. (9) to downward flows is tested as the first step to develop the interfacial area transport equation, and the correlation works well at the flow conditions where no group-II bubble is formed. However, as expected, once group-II bubbles are formed, the correlation tends to overestimate the interfacial area concentration significantly. Thus, the development of the interfacial area transport equation is recommended to predict such interfacial area transport process accurately.

4.4. Sauter mean diameter

Local bubble Sauter mean diameter, D_{Sm} profiles measured at $z/D = -13.0$, -68.0 and -133 are, respectively, depicted in the upper, middle and lower figures in Fig. 7. Axial developments of one-dimensional total interfacial area concentrations, $\langle D_{Sm}\rangle$, are also shown in Fig. 8. The meanings of the symbols are tabulated in Table 1. The lines in Fig. 8 indicate the values calculated by Eq. (9).

The bubble Sauter mean diameter profiles observed in the present experiments using a 25.4-mm diameter pipe are more or less similar to those in a 50.8-mm diameter pipe [12]. The bubble Sauter mean diameter profiles may be characterized as follows:

(1) The bubble Sauter mean diameters are almost uniform along the channel radius at the flow conditions where no group-II bubble is formed.
(2) No significant axial change is observed in the bubble Sauter mean diameter profile at the flow conditions where no group-II bubble is formed.
(3) Axial changes are observed in the bubble Sauter mean diameter profile at the flow conditions where group-II bubbles are formed ($\langle j_{g,0}\rangle = -0.289$ m/s and $\langle j_f\rangle = -1.25$ m/s, $\langle j_{g,0}\rangle = -0.381$ m/s and $\langle j_f\rangle = -2.12$ m/s, $\langle j_{g,0}\rangle = -0.487$ m/s and $\langle j_f\rangle = -3.11$ m/s).

The observations (1) and (2) may be approximately explained by the bubble interaction processes. Since the bubble interactions may not be so strong at such relatively low void fractions, the bubbles with approximately uniform size created at the inlet keep their size along the flow direction. As already explained in Sections 4.2 and 4.3, the observation (3) may be approximately explained by bubble interaction processes.

As shown in Fig. 8, insignificant axial changes of the one-dimensional bubble Sauter mean diameter are ob-

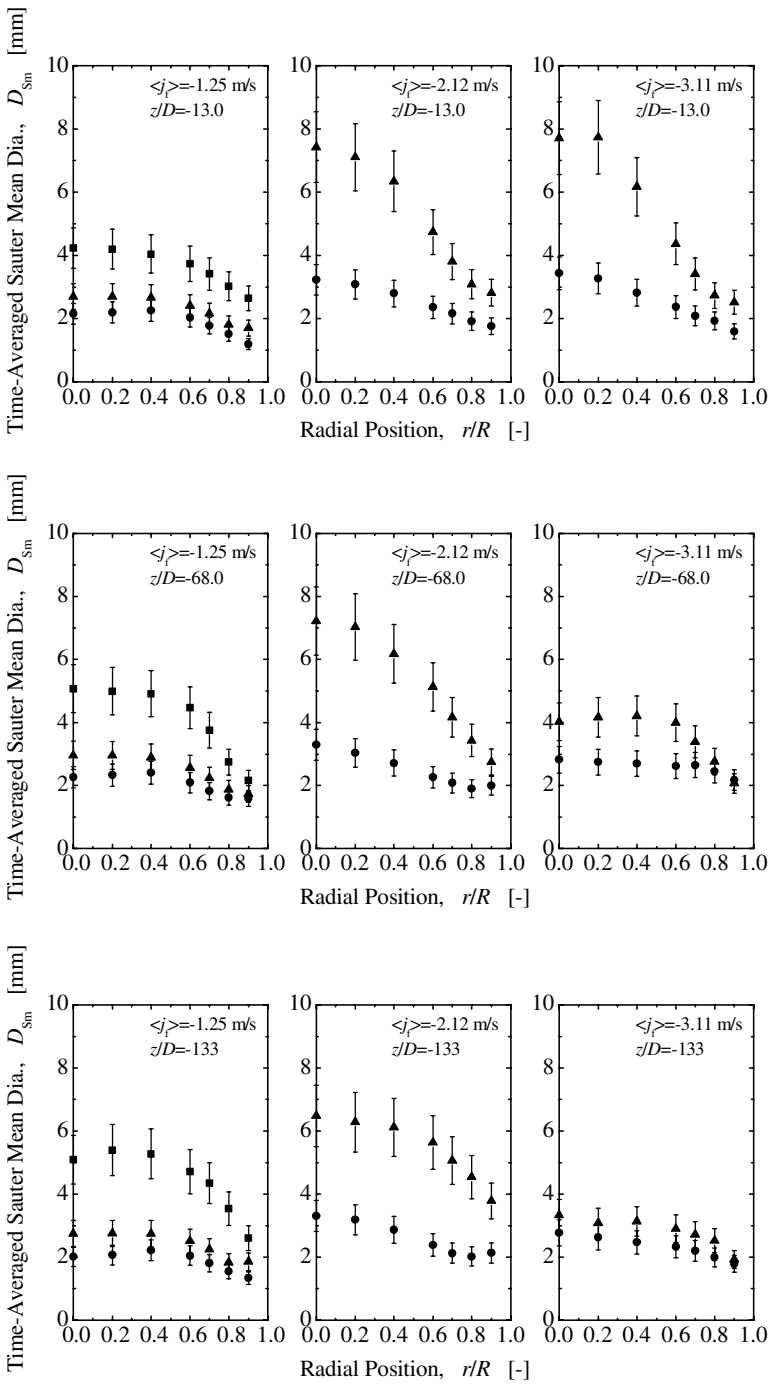

Fig. 7. Local bubble Sauter mean diameter profiles at $z/D = -13.0$, -68.0 and -133.

served at the flow conditions where no group-II bubble is formed, whereas significant axial changes of the one-dimensional bubble Sauter mean diameter are found depending on the liquid velocity at the flow conditions where group-II bubbles are formed. For relatively low liquid velocities such as $\langle j_f \rangle = -1.25$ m/s and $\langle j_f \rangle = -2.12$ m/s, the bubble Sauter mean diameters increase along the flow direction due to the bubble coalescence.

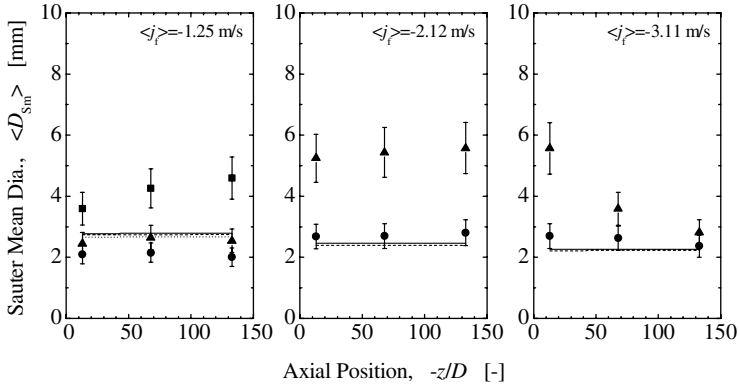

Fig. 8. Axial development of one-dimensional bubble Sauter mean diameter.

For relatively high liquid velocities such as $\langle j_f \rangle = -3.11$ m/s, the bubble Sauter mean diameters decreases along the flow direction due to the bubble disintegration. The applicability of the bubble Sauter mean diameter correlation given by Eq. (9) to downward flows is also tested, and the correlation works well at the flow conditions where no group-II bubble is formed. However, once group-II bubbles are formed, the correlation tends to underestimate the bubble Sauter mean diameter significantly. It is interesting to note that for $\langle j_{g,0} \rangle = -0.487$ m/s and $\langle j_f \rangle = -3.11$ m/s, the bubble Sauter mean diameter appears to approach the equilibrium value predicted for a fully-developed bubbly flow, and for $\langle j_{g,0} \rangle = -0.289$ m/s and $\langle j_f \rangle = -1.25$ m/s and $\langle j_{g,0} \rangle = -0.381$ m/s and $\langle j_f \rangle = -2.12$ m/s, the bubble Sauter mean diameters tend to deviate from their respective equilibrium values predicted for a fully-developed bubbly flow. These tendency indicates that the flows at $\langle j_{g,0} \rangle = -0.289$ m/s and $\langle j_f \rangle = -1.25$ m/s and $\langle j_{g,0} \rangle = -0.381$ m/s and $\langle j_f \rangle = -2.12$ m/s develop towards slug flow, and the flow at $\langle j_{g,0} \rangle = -0.487$ m/s and $\langle j_f \rangle = -3.11$ m/s develops toward bubbly flows, respectively. This may imply that the respective equilibrium flow regimes at the former and latter flow conditions are slug and bubbly flows, respectively.

4.5. Interfacial velocity

Local interfacial velocity, v_i profiles measured at $z/D = -13.0$, -68.0 and -133 are, respectively, depicted in the upper, middle and lower figures in Fig. 9. Axial developments of interfacial area concentration weighed cross-sectional area-averaged interfacial velocity, $\langle\langle v_i \rangle\rangle_a$, are also shown in Fig. 10. The meanings of the symbols are tabulated in Table 1. The lines in Fig. 10 indicate the values calculated by the drift-flux model given by Eqs. (6)–(8).

The interfacial velocity profiles observed in the present experiments using a 25.4-mm diameter pipe are more or less similar to those in a 50.8-mm diameter pipe [12]. The interfacial velocity profiles may be characterized as follows:

(1) The interfacial velocity profiles more or less display the power-law profiles.
(2) Small wall peaking phenomena are observed for $\langle j_{g,0} \rangle = -0.381$ m/s and $\langle j_f \rangle = -2.12$ m/s, $\langle j_{g,0} \rangle = -0.487$ m/s and $\langle j_f \rangle = -3.11$ m/s at $z/D = -13.0$.
(3) No significant axial change is observed in the interfacial velocity profiles.

The observation (1) may be approximately explained by the relationship between interfacial and liquid velocities. The interfacial velocity profiles are expected to be similar to the liquid velocity profiles. The interfacial velocity profiles at $\langle j_f \rangle = -1.25$ m/s are observed to be flatter than those at $\langle j_f \rangle = -2.12$ m/s and $\langle j_f \rangle = -3.11$ m/s. This may be attributed to the flatter liquid velocity profiles at $\langle j_f \rangle = -1.25$ m/s due to the bubble-induced turbulence. Since the shear-induced turbulence may be dominant at $\langle j_f \rangle = -2.12$ m/s and $\langle j_f \rangle = -3.11$ m/s, the interfacial velocity profiles at the flow conditions may be much parabolic in comparison with those at $\langle j_f \rangle = -1.25$ m/s.

The observation (2) may be approximately explained by bubbly "coring" effect. Wang et al. [24] reported the location of the maximum liquid velocity in downward bubbly flows occurred off the channel center in some flow conditions. The bubble "coring" in downward flows retarded the flow in the core due to buoyancy, and the resultant diversion of liquid into the low void region near the wall apparently caused the maximum liquid velocity to occur near the wall. As the void fractions around the channel center decrease along the flow direction, the local maxima in interfacial velocity profiles are disappeared. This may be a possible explanation for the observation (2).

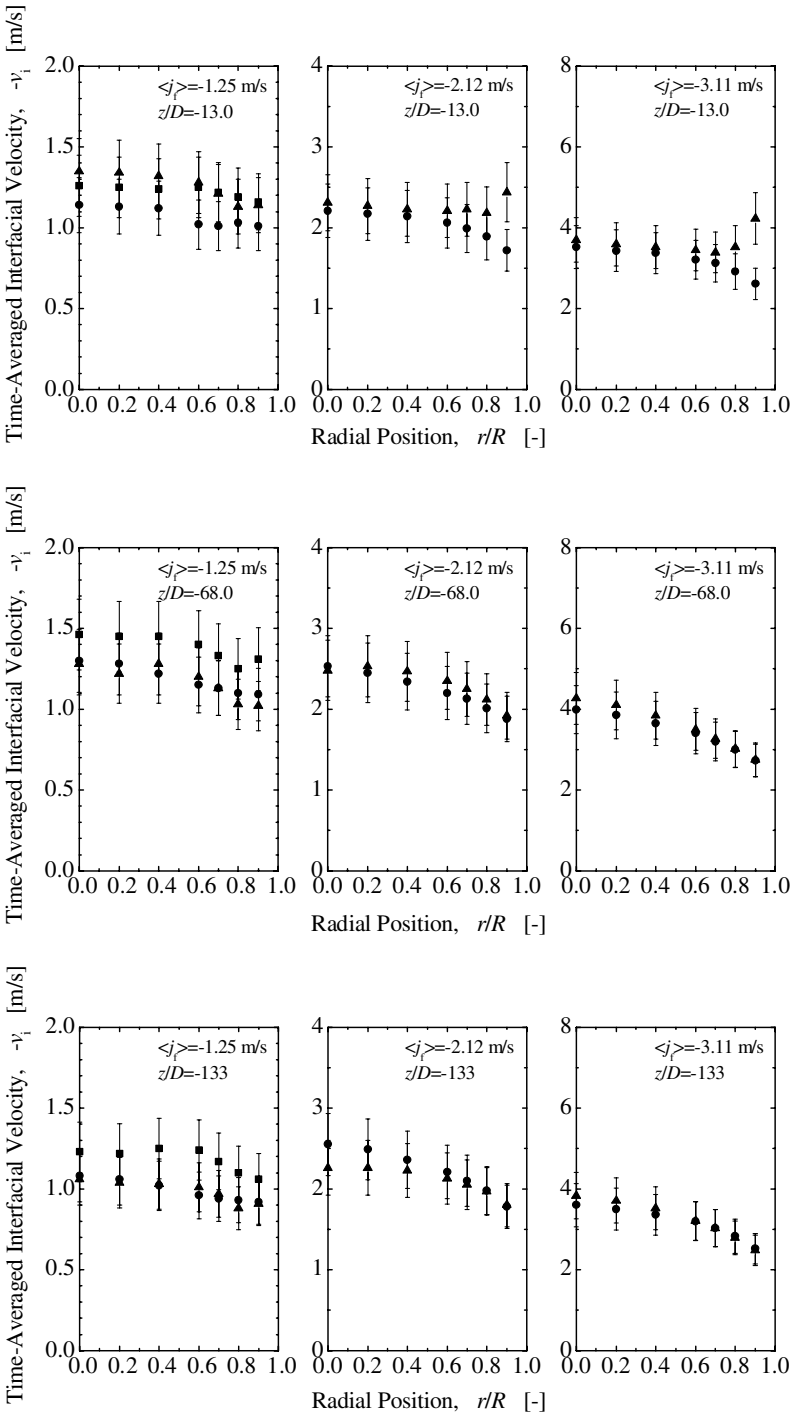

Fig. 9. Local interfacial velocity profiles at $z/D = -13.0$, -68.0 and -133.

As shown in Fig. 10, the axial changes of one-dimensional interfacial velocity are insignificant. Since the interfacial velocity, $\langle\langle v_i\rangle\rangle_a(\equiv\langle v_i a_i\rangle/\langle a_i\rangle)$ is approximated by $\langle\langle v_g\rangle\rangle(\equiv\langle v_g\alpha\rangle/\langle\alpha\rangle)$ in the bubbly flow regime [3,4], the drift-flux model given by Eqs. (6)–(8) also reproduce the axial developments of the interfacial velocity very well. The averaged prediction accuracy is estimated to be within ±9.47%. This indicates the drift-flux model

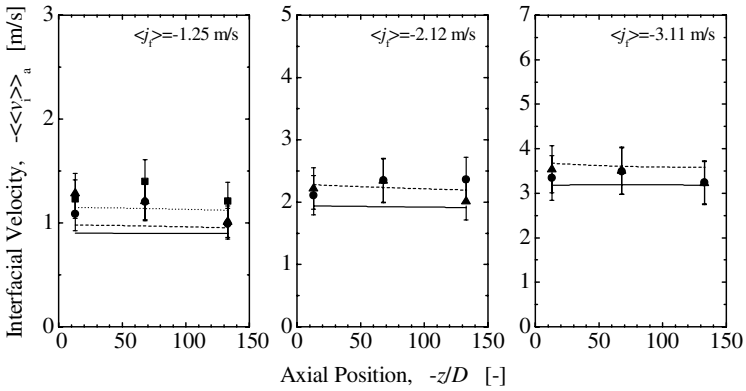

Fig. 10. Axial development of one-dimensional interfacial velocity.

given by Eqs. (6)–(8) can be applicable even to developing flows.

4.6. Dominant mechanism of interfacial area transport

As shown in Eq. (1), the axial change in the void fraction affects the interfacial area transport along the flow direction. In order to examine the dominant mechanism of the interfacial area transport, a parameter, ξ, defined by $\langle a_i \rangle / \langle a_{i,\mathrm{eq}} \rangle$ is introduced, where $a_{i,\mathrm{eq}}$ is the interfacial area concentration under the conditions of no phase change and equilibrium of bubble coalescence and breakup rates. Thus, the parameter, ξ, indicates the ratio of the actual interfacial area transport to the interfacial area transport only due to the void fraction change as an index of the net interfacial area transport due to the bubble coalescence and breakup. $\xi > 1$ or $\xi < 1$ corresponds to the bubble breakup or coalescence dominant flow. The parameter can be derived analytically from Eq. (4) with the assumptions of insignificant axial changes of v_i and v_g and $v_i \approx v_g$ as

$$\xi \equiv \frac{\langle a_i \rangle}{\langle a_{i,\mathrm{eq}} \rangle} = \frac{\int_A a_i \, \mathrm{d}A}{\int_A \left(\frac{\alpha}{\alpha^+}\right)^{2/3} a_i^+ \, \mathrm{d}A}, \tag{12}$$

where A is the area of the flow channel, and the superscript + means the reference axial location. In the calculation, $z/D = -13.0$ is used as the reference axial location, and the interfacial area transport between $z/D = -13.0$ and -133 is examined.

The upper and lower figures in Fig. 11 show the dependences of the parameter, ξ, on the void fraction at $z/D = -13.0$ and the superficial liquid velocity, respectively. Open symbols in the upper figure indicate the calculated parameters. Lines in the lower figure indicate the parameters reproduced by the interpolation of the data shown in the upper figure. As can be seen from the upper figure, the increase in the void fraction enhances the dominant interfacial area transport mechanism, namely

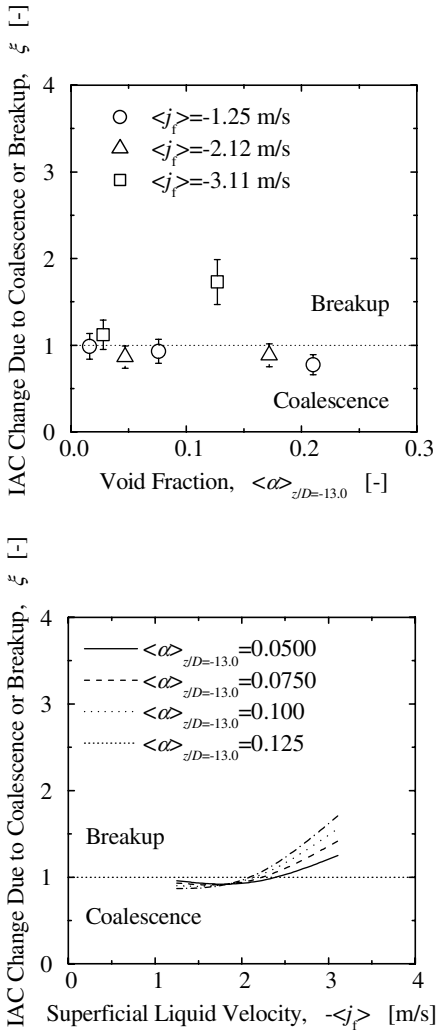

Fig. 11. Dependence of interfacial area transport due to bubble coalescence and breakup on void fraction.

bubble coalescence at $\langle j_f \rangle = -1.25$ and -2.12 m/s, and bubble breakup at $\langle j_f \rangle = -3.11$ m/s. The lower figure also shows that the dominant interfacial area transport mechanism is bubble coalescence or breakup at the superficial liquid velocity lower or higher than 2 m/s, respectively. Thus, the interfacial area transport mechanism is dependent on the void fraction, liquid turbulence, and possibly bubble size. This suggests that the source and sink terms should be modeled by taking account of the void fraction, liquid turbulence and bubble size [3–6]. The data sets of downward flows obtained in this study using a 25.4-mm diameter pipe together with those in our previous study using a 50.8-mm diameter pipe [12] will be used for the development of reliable constitutive relations such as the interfacial area transport equation.

5. Conclusions

Accurate prediction of the interfacial area concentration is essential to successful development of the interfacial transfer terms in the two-fluid model. Mechanistic modeling of the interfacial area concentration entirely relies on accurate local flow measurements over extensive flow conditions and channel geometries. From this point of view, accurate measurements of flow parameters such as void fraction, interfacial area concentration, bubble Sauter mean diameter, and interfacial velocity were performed by a multi-sensor probe in vertical downward bubbly flows using a 25.4 mm-diameter pipe. The obtained results are summarized as follows:

(1) The local measurements were performed at three axial locations of $z/D = -13.0$, -68.0 and -133 as well as seven radial locations from $r/R = 0$ to 0.9 using a multi-sensor probe. A total of 7 data sets were acquired consisting of 147 (= 7 flow conditions × 7 radial locations × 3 axial locations) local data points. The flow conditions cover the void fractions from 1.61% to 21.0% and the superficial liquid velocities from -1.25 to -3.11 m/s.
(2) The phenomena characterizing the downward bubbly flows were discussed in detail. The mechanisms of the radial profiles of local flow parameters and their axial developments were briefly discussed.
(3) The existing drift-flux model was compared with the measured one-dimensional data. It reproduced the axial developments of the void fraction and interfacial velocity very well. The averaged prediction accuracies of one-dimensional void fraction and interfacial velocity were estimated to be within ±9.66% and ±9.47%, respectively.
(4) The existing interfacial area correlation was compared with the measured one-dimensional data. It reproduced the axial developments of the interfacial area concentration very well at the flow conditions where no group-II bubble was formed. However, once group-II bubbles were formed, the correlation tended to overestimate the interfacial area concentration significantly. Thus, the development of the interfacial area transport equation was recommended to predict such interfacial area transport process accurately.
(5) The dominant interfacial area transport mechanism was displayed as functions of void fraction and superficial liquid velocity. The interfacial area transport was expected to be expressed as functions of void fraction, superficial liquid velocity, and possibly bubble size.

Acknowledgment

This work was supported by the USNRC Office of Nuclear Regulatory Research.

References

[1] M. Ishii, Thermo-Fluid Dynamic Theory of Two-Phase Flow, Eyrolles, Paris, 1975.
[2] G. Kocamustafaogullari, M. Ishii, Foundation of the interfacial area transport equation and its closure relations, Int. J. Heat Mass Transfer 38 (1995) 481–493.
[3] Q. Wu, S. Kim, M. Ishii, S.G. Beus, One-group interfacial area transport in vertical bubbly flow, Int. J. Heat Mass Transfer 41 (1998) 1103–1112.
[4] T. Hibiki, M. Ishii, One-group interfacial area transport of bubbly flows in vertical round tubes, Int. J. Heat Mass Transfer 43 (2000) 2711–2726.
[5] T. Hibiki, M. Ishii, Two-group interfacial area transport equations at bubbly-to-slug flow transition, Nucl. Eng. Des. 202 (2000) 39–76.
[6] X.Y. Fu, M. Ishii, Two-group interfacial area transport in vertical air-water flow I. Mechanistic model, Nucl. Eng. Des. 219 (2000) 143–168.
[7] T. Hibiki, S. Hogsett, M. Ishii, Local measurement of interfacial area, interfacial velocity and liquid turbulence in two-phase flow, Nucl. Eng. Des. 184 (1998) 287–304.
[8] T. Hibiki, M. Ishii, Experimental study on interfacial area transport in bubbly two-phase flows, Int. J. Heat Mass Transfer 42 (1999) 3019–3035.
[9] T. Hibiki, M. Ishii, Z. Xiao, Axial interfacial area transport of vertical bubbly flows, Int. J. Heat Mass Transfer 44 (2001) 1869–1888.
[10] X.D. Sun, T.R. Smith, S. Kim, M. Ishii, J. Uhle, Interfacial area of bubbly flow in a relatively large diameter pipe, Exp. Thermal Fluid Sci. 27 (2002) 97–109.
[11] T. Hibiki, R. Situ, Y. Mi, M. Ishii, Experimental study on interfacial area transport in vertical upward bubbly two-phase flow in an annulus, Int. J. Heat Mass Transfer 46 (2003) 427–441.

[12] T. Hibiki, H. Goda, S. Kim, M. Ishii, J. Uhle, Experimental study on interfacial area transport of a vertical downward bubbly flow, Exp. Fluids 35 (2003) 100–111.
[13] S. Kim, X.Y. Fu, X. Wang, M. Ishii, Development of the miniaturized four-sensor conductivity probe and the signal processing scheme, Int. J. Heat Mass Transfer 43 (2000) 4101–4118.
[14] T. Takamasa, T. Goto, T. Hibiki, M. Ishii, Experimental study of interfacial area transport of bubbly flow in small-diameter tube, Int. J. Multiphase Flow 29 (2003) 395–409.
[15] M. Ishii, N. Zuber, Drag coefficient and relative velocity in bubbly, droplet or particulate flows, AIChE J. 25 (1979) 843–855.
[16] T. Hibiki, H. Goda, S. Kim, M. Ishii, J. Uhle, Structure of vertical downward bubbly flow, Int. J. Heat Mass Transfer 47 (2004) 1847–1862.
[17] H. Goda, T. Hibiki, S. Kim, M. Ishii, J. Uhle, Drift-flux model for downward two-phase flow, Int. J. Heat Mass Transfer 46 (2003) 4835–4844.
[18] T.R. Auton, The lift force on a spherical body in a rotational flow, J. Fluid Mech. 183 (1987) 199–218.
[19] D.A. Drew, R.T. Lahey Jr., The virtual mass and lift force on a sphere in rotating and straining inviscid flow, Int. J. Multiphase Flow 13 (1987) 113–121.
[20] S.P. Antal, R.T. Lahey Jr., J.E. Flaherty, Analysis of phase distribution in fully developed laminar bubbly two-phase flow, Int. J. Multiphase Flow 17 (1991) 635–652.
[21] R.T. Lahey Jr., M. Lopez de Bertodano, O.C. Jones Jr., Phase distribution in complex geometry conduits, Nucl. Eng. Des. 141 (1993) 177–201.
[22] O.N. Kashinsky, V.V. Randin, Downward bubbly gas–liquid flow in a vertical pipe, Int. J. Multiphase Flow 25 (1999) 109–138.
[23] T. Hibiki, M. Ishii, Interfacial area concentration of bubbly flow systems, Chem. Eng. Sci. 57 (2002) 3967–3977.
[24] S.K. Wang, S.J. Lee, O.C. Jones Jr., R.T. Lahey Jr., 3-D turbulence structure and phase distribution measurements in bubbly two-phase flows, Int. J. Heat Mass Transfer 13 (1987) 327–343.